Nano Research

Open Access

Research Article

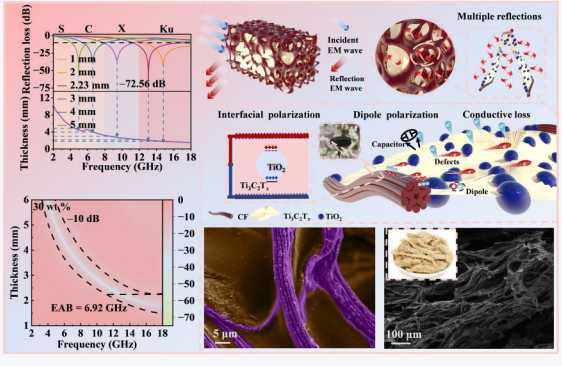
Micro-macro regulating heterogeneous interface engineering in 3D N-doped carbon fiber/MXene/TiO_2 nano-aerogel for boosting electromagnetic wave absorption

Ying Li[1,2], Chunlei Dong[1], Sijia Wang[1], Dongyi Lei[1,2] ✉, Binbin Yin[3], Yifei Cui[1,2], Yanru Wang[1,2], and Ran Li[1,2]

[1] *School of Civil Engineering, Qingdao University of Technology, Qingdao 266033, China*
[2] *Cooperative Innovation Center of Engineering Construction and Safety in Shandong Blue Economic Zone, Qingdao University of Technology, Qingdao 266033, China*
[3] *Department of Architecture and Civil Engineering, City University of Hong Kong, Hong Kong 999077, China*

Cite this article: *Nano Research*, **2025**, *18*, 94907169. https://doi.org/10.26599/NR.2025.94907169

ABSTRACT: MXene, as a rising star among two-dimensional (2D) electromagnetic wave materials, faces urgent challenges in addressing its self-stacking issue and regulating its conductivity. Herein, a micro-macro collaborative design strategy was proposed to regulate heterogeneous interface engineering in MXene-based absorbers. Biomass-based cotton was introduced as three-dimensional (3D) framework for constructing a porous structure, TiO_2 was *in-situ* generated and nitrogen atom was doped on $Ti_3C_2T_x$ MXene to regulate its dielectric properties, a 3D N-doped carbon fiber/MXene/TiO_2 (CMT) nano-aerogel was successful constructed. The synergistic effects of diverse components and structural designs, porous frameworks and TiO_2 lattice contraction can significantly adjust the density of the conductive network and create abundant heterogeneous interfaces, as well as the lattice defects induced by nitrogen atom doping can enhance polarization loss, ultimately leading to the excellent microwave absorption performance of 3D N-CMT nano-aerogels. The optimized N-CMT 30% aerogel exhibited a minimum reflection loss (RL_{min}) of −72.56 dB and an effective absorption bandwidth (EAB) of 6.92 GHz at 2.23 mm. Notably, when the thickness was adjusted from 1 to 5 mm, the EAB of the N-CMT 30% aerogel reached 13.94 GHz, achieving coverage of 98% of the C-band and the entire X and Ku bands. Furthermore, the attenuation capabilities of the N-CMT aerogel were further confirmed through RCS simulations, whose RCS reduction value reaches up to 19.969 dB·m². These results demonstrate that 3D N-CMT nano-aerogel relying on interface engineering design exhibits significant potential in the field of electromagnetic protection, providing an important reference for future efficient absorbers.



KEYWORDS: interface engineering, electromagnetic wave absorption, MXene, micro-macro design, nano-aerogel

1 Introduction

The widespread application of 5G technology and the rapid iterative updates of electronic devices have led to increasing electromagnetic pollution, posing a significant threat to national security and human health [1–4]. Therefore, it is necessary to design and explore ideal electromagnetic absorption (EMA) materials that meet the requirements of thin thickness, light weight, wide absorption bandwidth, and strong reflection loss. Recently, the design and preparation of efficient microwave absorbers mainly focus on the construction of reasonable heterogeneous structures and development of multi-component microwave absorbers [5–7]. In general, the characteristics of heterogeneous interfaces are controlled by the Maxwell–Wagner effect, with applications ranging from the macroscopic to the nanoscale, thus influencing dielectric and magnetic properties such as band alignment [8], spatial charge distribution [9], electron transport [10], and lattice defects [11]. Rational design of heterogeneous structures can optimize the interfacial area and interfacial effects, while concurrent design of multiple components and structures can achieve efficient interfacial control. Therefore, heterogeneous interface engineering by modulating both impedance matching and energy dissipation

Received: August 16, 2024; **Revised:** November 20, 2024
Accepted: December 2, 2024

✉Address correspondence to leidongyi@qut.edu.cn

has become a hot strategy recently for designing materials with high-efficiency microwave absorption properties [12].

MXene refers to a series of novel two-dimensional (2D) transition metal carbides/nitrides/carbonitrides, which boasts hydrophilic properties, and tunable conductivity, typically prepared through the selective etching of metal layers from MAX phase precursors [13, 14]. The abundant surface functional groups (–OH, –O, and/or –F groups) on MXene nanosheets provide significant dipole and interfacial polarization, facilitating their connection with other materials and thus demonstrating tremendous potential in the design of heterogeneous interfaces [15]. However, the surface of conductive MXene is rich in free electrons, which causes electromagnetic waves to reflect off the surface rather than enter the absorber, thereby affecting the absorption efficiency. To address this case, two effective strategies have been explored from a microscopic perspective. First of all, the facile oxidation properties of $Ti_3C_2T_x$ can be cleverly exploited to perform *in-situ* design of MXene from the perspective of interface engineering. Thermal annealing treatment is applied to $Ti_3C_2T_x$ MXene nanosheets to induce in-situ derivation of TiO_2 and construct heterojunction interfaces, which has become a significant strategy to prepare outstanding microwave absorbing candidates. Yin's team [17] proposed that annealed $Ti_3C_2T_x$ under an Ar atmosphere at 800 °C maintains their original layered morphology, as well as induces the production of TiO_2 nanocrystals and amorphous carbon, enhancing the dielectric properties and thus improving its EMA performance. A 50 wt.% $Ti_3C_2T_x$/paraffin composite achieved a RL_{min} value of −48.4 dB at 11.6 GHz with a thickness of 1.7 mm. Additionally, they also studied the influence of annealing treatment under CO_2 atmosphere on the electromagnetic properties of $Ti_3C_2T_x$ [18]. After thermal annealing, the multilayered $Ti_3C_2T_x$ nanosheets transformed into a partially ordered layered structure composed of defective 2D carbon layers and TiO_2 flakes, effectively improving their dielectric properties. The C/TiO_2/paraffin composite with 55 wt.% and 45 wt.% exhibit a minimum reflection loss (RL_{min}) of −50.3 dB at 7.1 GHz and an EAB of 5.6 GHz with a thickness of 1.7 mm, respectively. TiO_2 sheets with a low dielectric constant improve the impedance matching of the composites. Meanwhile, the 2D carbon layers induce orientation polarization in alternating electromagnetic fields due to their disordered nature and high concentration of structural defects and oxygen functional groups. Additionally, the uniform embedding of TiO_2 sheets within the carbon layers prevents their aggregation and forms heterogeneous interfaces and capacitive-like structures, thereby enhancing polarization losses and electromagnetic wave dissipation. Therefore, construction of heterogeneous interface engineering by *in-situ* generated TiO_2 on the multilayered $Ti_3C_2T_x$ by annealing treatment is an effective approach to enhancing its dielectric properties.

The other significant strategy is that introduction of heteroatom into $Ti_3C_2T_x$ MXene to improve its electromagnetic properties. Inserting nitrogen atoms into the $Ti_3C_2T_x$ lattice can introduce defects and broaden the bandgap, resulting in reduced conductivity and fewer charge carriers [16]. The N-$Ti_3C_2T_x$ biphasic structure contains numerous nitrogen doping defects, leading to the deviation of the symmetric centers of carbon and nitrogen atoms from their original positions, leading to dipole polarization. Nitrogen can be introduced using urea-saturated alcohol solution, monoethanolamine [17], sodium citrate [18], glycine [19], etc., as nitrogen sources. However, these methods often suffer from issues such as low doping levels, high defect density, poor stability, and uneven distribution of heteroatoms [20]. In view of this, direct carbonization of nitrogen-containing polymers (e.g., polyimide [21], polyvinylpyridine, polyacrylonitrile [22], polyaniline [23], etc.) can be used to improve the impedance matching, interfacial polarization, and dipole polarization of N-MXene. One important reason for selecting polyimide as the nitrogen source is that the polyamic acid (the precursor of polyimide) molecules contain abundant of carboxyl, secondary amine, and primary amine groups, which can react with the surface groups of MXene, enabling more effective crosslinking with MXene [24, 25]. Chen et al. used the carbonization method to coat the polyimide with a nitrogen-doped carbon layer on the surface of graphene. The prepared nitrogen-doped carbon-coated graphene (NCG) exhibits excellent capacitive performance as a supercapacitor, but there is little existing research applied in the field of wave absorption [20].

Moreover, due to the interaction between hydrogen bonding and van der Waals forces, MXene is also restricted by self-stacking between layers, so designing a reasonable heterostructure remains challenging [26]. To inhibit their self-stacking, constructing a three-dimensional porous structure from a macroscopic perspective is an attracting approach. Nevertheless, MXene-based composites generally exhibit poor mechanical strength when constructing 3D porous structures through van der Waals forces, which cannot maintain an independent configuration owing to their weak interlayer interactions [27, 28]. Therefore, the preparation of 3D MXene-based microwave absorbing materials with certain mechanical properties and efficient EMA performance is currently an urgent issue to be addressed. It is well-known that biomass cotton fiber is a sustainable and economically accessible carbon material. The use of lightweight absorbent cotton balls as precursors can effectively retain the porous microstructure through carbonization, which not only satisfies the demand for lightness but also allows the presence of 3D pores to extend the propagation path of EMW reflection and scattering, thus attenuating electromagnetic energy [29]. In addition, the high porosity of biomass cotton fiber offers sufficient space for the loading of nanoparticles and nanosheets. Wang et al. [30] coupled carbon nanotubes (CNTs) derived from Co-ZIF arrays onto a cotton fiber (CF)-supported MXene shell (Co/CNTs-MXene@CF). The Co/CNTs-MXene@CF heterogeneous structure exhibited a RL_{min} of 61.41 dB at 2.52 mm, with an EAB reaching 5.04 GHz at a thickness of 1.5 mm.

Herein, a biomass-based cotton as 3D porous framework and $Ti_3C_2T_x$ MXene and PAA were introduced to fabricate 3D interconnected loofah-like N-CMT nano-aerogel through micro-macro collaborative design strategy. After thermal annealing at 700 °C under N_2, TiO_2 nanoparticles and layered carbon layers were *in-situ* generated within the MXene nanosheets and CF to construct abundant heterogeneous interfaces. Macroscopically, the introduction of cotton derived carbon fibers created porous structures, facilitating multiple reflections of incident electromagnetic waves within the pores and connecting adjacent MXene units to form an intertwined conductive network. Microscopically, from the perspective of interface engineering, the lattice defects of TiO_2 nanoparticles with low dielectric constant lead to the contraction of crystal cells, thereby improving the dielectric loss capability. Moreover, TiO_2 and MXene can generate additional heterojunction interfaces to enhance interface polarization. Notably, PAA decomposition introduced more nitrogen doping defects, enhancing dipolar polarization, resulting in the excellent electromagnetic wave absorption performance of N-CMT nano-aerogel. Regulation of interface engineering in a three-dimensional nano-aerogel from microscopic and macroscopic

perspectives, providing a promising strategy for constructing absorbers with highly efficient microwave absorption properties.

2 Experimental section

2.1 Materials

Ti_3AlC_2 MAX phase (400 mesh) was provided by Jilin 11 Technology (Co., Ltd., China). 4,4'-Oxydianiline (4,4'-ODA) and N,N-dimethylacetamide (DMAc) were purchased from Shanghai Aladdin Co., Ltd. Triethylamine (TEA, 99.0%), pyromellitic dianhydride (PMDA, 96.0%), and lithium fluoride (LiF, 99.9%) were procured from Macklin Chemical Reagent Co., Ltd. Hydrochloric acid (HCl, 37.0%) was provided by Sinopharm Chemical Reagent (Co., Ltd., China). All the chemicals were used without further purification. Additionally, the absorbent cotton balls and the deionized water were bought from local chemical agent company.

2.2 Synthesis of $Ti_3C_2T_x$ MXene

Initially, $Ti_3C_2T_x$ was obtained through selective etching of the Al atomic layer of Ti_3AlC_2 through the reaction of HCl and LiF. Detailed procedures were outlined as follows: A mixture of 1 g of LiF and 30 mL of HCl (9 M) were magnetically stirred in a Teflon beaker to achieve homogeneity. Then, 1 g of Ti_3AlC_2 powder was added, and the reaction was carried out at 40 °C for 24 h. After the reaction, the mixed solution was centrifuged with deionized water (3500 rpm, 5 min per cycle) until the pH reaches 6. The precipitate obtained through centrifugation was dispersed in 50 mL of deionized water and sonicated in an ice bath under N_2 atmosphere for 60 min. Centrifuge the sonicated solution for 75 min at 3500 rpm, and collect the supernatant. Ultimately, the supernatant was frozen at −20 °C and subjected to freeze-drying to yield MXene nanosheet powder.

2.3 Preparation of water-soluble polyamic acid (PAA)

Firstly, 1.982 g of 4,4'-ODA and 50 mL of DMAc were uniformly mixed under magnetic stirring, and then 2.181 g of PMDA was slowly added to the above solution. After reacting for 8 h, transfer the solution into 500 mL of deionized water. This will result in a flocculent precipitate. Wash the precipitate with deionized water to yield a lightly yellowed polymer solid and dry the solid at 50 °C. Subsequently, combine 1 g of the dried material with 18.5 g of deionized water and add 0.5 g of TEA. Stir the mixture magnetically at room temperature until it becomes clear to result in a 5 wt.% PAA solution.

2.4 Preparation of N-CMT nano-aerogel

In detail, the $Ti_3C_2T_x$ MXene nanosheets were utilized to prepare a 10 mg/mL MXene suspension. The construction of 3D N-CMT (N-doped CF/MXene/TiO_2) nano-aerogel was achieved through direct freeze-drying and thermal annealing. Firstly, similar to our previous work, the prepared $Ti_3C_2T_x$ aqueous suspension was mixed with a water-soluble polyimide precursor solution, with MXene mass ratios of 5%, 15%, 30%, and 45%. A homogeneous dispersion was then obtained through ultrasonic dispersion and magnetic stirring. Absorbent cotton balls were immersed in the mixed solution for 48 h under vacuum conditions. After freezing the cotton balls impregnated with the mixed solution for 12 h, vacuum freeze-drying was performed for 72 h to obtain the CF/MXene/PAA composite sponge. Finally, the obtained composite aerogel was thermally annealed under nitrogen atmosphere at 700 °C for 2 h, resulting in a 3D interconnected loofah-like N-doped CF/MXene/TiO_2 nano-aerogel.

2.5 Characterization

The microstructure of the samples was characterized using field emission scanning electron microscopy (FE-SEM, Sigma300) and high-resolution transmission electron microscopy (HRTEM, JEM-2100F). The phase composition of the sample was characterized using an X-ray diffractometer (XRD, Rigaku SmartLab). The instrument was operated under conditions of 40 kV voltage and 40 mA current, scanning at a rate of 5 °/min within a range of 5° to 90°. To investigate the graphitization degree of the aerogel, Raman spectroscopy tests were conducted on the absorbent cotton and N-CMT 30%. The bonding and valence states of the surface components of the sample were determined using X-ray photoelectron spectroscopy (XPS, Thermo Fisher Scientific K-Alpha) with an Al Kα radiation source, a tube voltage of 15 kV, a tube current of 10 mA, and an X-ray energy of 1486.8 eV. For fine spectrum testing, a step size of 0.05 eV and a scan count of 3–5 times were typically used, with the analysis mode set to CAE mode and a pass energy of 30.0 eV. For full spectrum testing, a step size of 1 eV, a binding energy range of −5 to 1350 eV, a pass energy of 150 eV, and a scan count of 1 were used. Etching was performed using an Ar^+ gun at a beam energy of 2 kV and a medium beam current (10 mA), with an etching rate of typically 0.2 nm/s. The instrument had a work function of 4.2 eV and was equipped with a neutralizing gun to eliminate charge accumulation (calibration typically used the binding energy of 284.8 eV for the C 1s orbital). The parameters of the macropores (> 50 nm) in the sample were determined using mercury intrusion porosimetry (PoreMaster 33, Quantachrome), and the nitrogen adsorption and desorption isotherms were measured using a SAP 2020HD88 analyzer. The specific surface area of the sample was determined using the BET method, and the micropore size distribution (< 50 nm) was determined using the BJH method. Thermogravimetric analysis (TGA) was conducted using a thermogravimetric analyzer (TG 209F1) in nitrogen atmosphere, with a heating rate of 10 °C/min from room temperature to 800 °C. To prepare the concentric ring, the paraffin was melted at 80 °C, and then poured into the aerogel interior (N-CMT 5%, N-CMT 15%, N-CMT 30% and N-CMT 45%) with the assistance of vacuum. After cooling, press the sample in a mold to form a ring with an outer diameter of 7 mm and an inner diameter of 3.04 mm for testing. Test the electromagnetic parameter of complex permittivity ($\varepsilon_r = \varepsilon' - j\varepsilon''$) and complex permeability ($\mu_r = \mu' - j\mu''$) of the sample within the frequency range of 2–18 GHz using a network analyzer (Agilent Technologies N5222A). RL curves were determined with the measured ε_r and μ_r based on the transmission line theory RL equation.

3 Results and discussion

3.1 Composition and structure

To date, various biomass materials have been utilized as templates for the preparation of microwave absorbing materials (MAMs), encompassing pumpkin seed shells [31], discarded rice husks [32], pomelo peels [33], corn stalks [34], and loofah sponges [35]. Despite the easy availability of these raw materials, the current biomass-derived carbon materials fail to meet the requirements of being lightweight, thin, broadband, and strong due to their limited

electromagnetic (EM) dissipation capabilities. Consequently, the development of composites with enhanced EM performance, composed of biomass-derived materials and other nano-absorbing materials, has emerged as a research hotspot [33]. Figure 1 illustrates the preparation process of N-CMT nano-aerogel, with the macro- and micro-level design concepts described as follows. Initially, the Al layer of Ti_3AlC_2 MAX phase was etched using LiF and HCl to obtain multi-layer $Ti_3C_2T_x$, which was then stripped through ultrasonic treatment to yield single-layer/few-layer $Ti_3C_2T_x$ MXene sheets. Macroscopically, green and low-cost biomass cotton was employed as the matrix to provide a 3D skeletal structure, effectively mitigating the self-stacking of MXene and enhancing multiple reflections and scattering of electromagnetic waves within the internal structure. Subsequently, interface engineering was further constructed at the microscale. The *in-situ* formed TiO_2 brought multi-component heterogeneous interfaces, thereby improving the dielectric properties of $Ti_3C_2T_x$. Simultaneously, the carbonization of polyimide introduced nitrogen elements, and lattice defects induced by nitrogen doping enhanced polarization losses. The introduced N atoms and expanded interlayer spacing provided structural features conducive to achieving dielectric loss [16]. Apparently, the 2D MXene sheets and in-situ derived TiO_2 particles were interleaved among one-dimensional carbon fibers, jointly constructing a 3D porous structure. The unique structural features and abundant heterogeneous interfaces would endow the 3D N-doped CF/MXene/TiO_2 nano-aerogel with excellent electromagnetic wave absorption performance. Additionally, 3D N-CMT nano-aerogel utilizing biomass cotton as its matrix, achieves a lightweight characteristic with a density of only 0.048 g/cm^3. Compared to other reported low-density absorbing materials, it realizes stronger absorption and wider bandwidth at even lower densities (Fig. S1 and Table S1 in the Electronic Supplementary Materials (ESM)). To better investigate its mechanical properties, compression tests with different strains ranging from 10% to 60% were conducted on pure cotton and 3D N-CMT nano-aerogels with varying proportions at a compression rate of 5 mm/min. As shown in Fig. S2 in the ESM, the N-CMT nano-aerogel exhibits excellent mechanical robustness.

The SEM images of 3D N-CMT nano-aerogel under high and low magnifications are presented in Figs. 2(a) and 2(b), and 2(c) and 2(d), respectively. The macroscopic structure of the material exhibits a regular and dense wrinkled layer-like structure resembling a loofah sponge. It can also be observed that the morphology of the MXene nanosheets remains intact after annealing, indicating that the thermal annealing treatment did not significantly damage the overall structure. The carbon fibers connect multiple components in the MXene/TiO_2 composite, forming a conductive network that accelerates electron transfer and enhances conductivity. The loofah-like structural network can effectively improve the multiple reflections and attenuation of electromagnetic waves, generating more heterogeneous interfaces, making it a significant scattering loss absorber (Figs. 2(c), 2(d) and 2(h)). To further investigate the microstructure of 3D N-CMT nano-aerogels, the macropores (> 50 nm) and micropores (< 50 nm) of the samples were analyzed using mercury intrusion porosimetry and nitrogen gas adsorption methods, respectively. On one hand, the pore size distribution of the micropores (< 50 nm) in 3D N-CMT nano-aerogels with different proportions was determined by the Brunauer–Emmett–Teller (BET) gas adsorption method [36, 37]. Figure S3 in the ESM depicts the nitrogen adsorption-desorption curves for four proportions of 3D N-CMT nano-aerogels. The typical type IV isotherm, observed from the nitrogen adsorption-desorption isotherms, characterizes their porosity. As the relative pressure increases, the N_2 adsorption curve begins to rise slowly, indicating the presence of micropores in the 3D N-CMT nano aerogels. When the relative pressure reaches 0.85 P/P_0, the N_2 adsorption curve starts to rise sharply, suggesting the existence of mesopores and macropores in the composite aerogels [38, 39], as shown in Figs. S3(a_1)–S3(d_1) in the ESM. As illustrated in Fig. S4(a) in the ESM, the mercury intrusion-extrusion curve demonstrates that the mercury intrusion volume rapidly increases with the applied pressure. However, when the pressure reaches 10 pisa, there is virtually no change in the mercury intrusion volume, indicating that the interior of the aerogel is primarily composed of macropores.

This observation is corroborated by the pore size distribution curve shown in Fig. S4(b) in the ESM. The porosity of the N-CMT 45% 3D nano-aerogel is 87.5359%, with a total mercury intrusion



Figure 1 Schematic illustration of the preparation process of 3D N-CMT nano-aerogel.

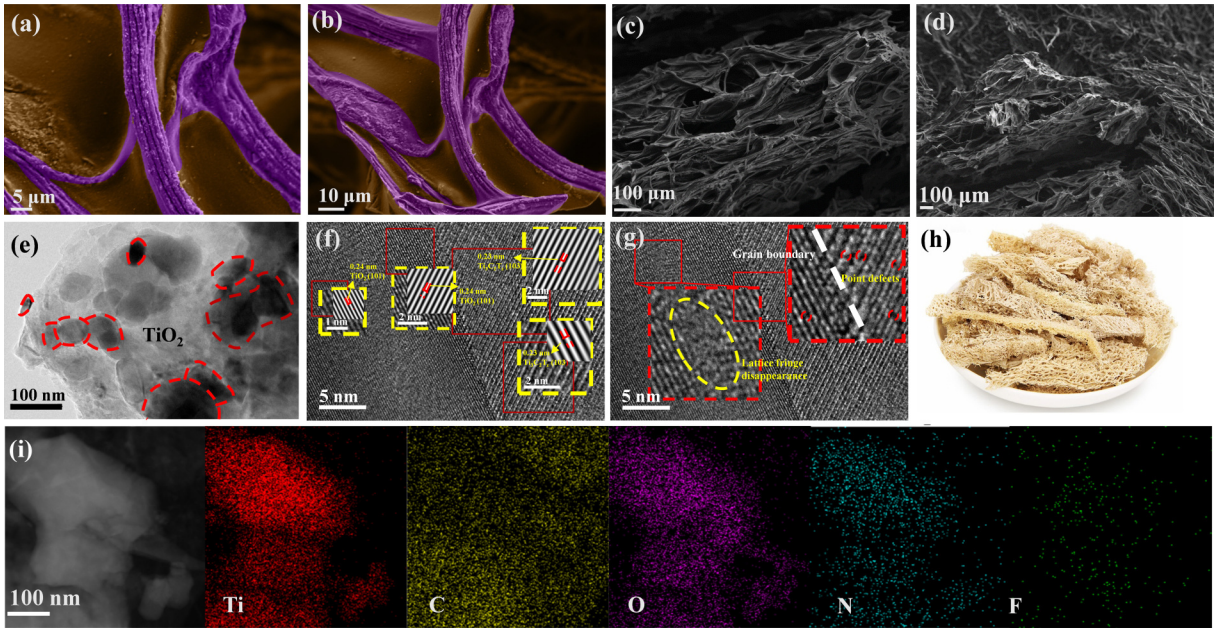


Figure 2 (a)–(d) SEM images, (e)–(g) TEM images, (h) biomimetic image, and (i) EDS images of Ti, C, O, N, and F of N-CMT 30% aerogel.

volume of 10.6532 mL/g, and the pore sizes are mainly distributed within the range of 10 to 500 μm (Table S2 in the ESM). Figure 2(e) presents the TEM image of the 3D N-CMT nano-aerogel, showcasing distinct edge structures that signify robust interfacial adhesion among them. The MXene exhibits good electronic transparency, indicating that the thin walls consist of several layers of $Ti_3C_2T_x$ sheets [40]. From a microscopic perspective, irregular TiO_2 particles can be observed that has been *in-situ* generated on the MXene nanosheets, which is conductive to regulate the conductivity network density of 3D N-CMT nano-aerogel. Furthermore, Fig. 2(i) analyzes the EDS elements of the composite material, revealing the presence of Ti, C, O, N, F, and other elements in the N-CMT nano-aerogel. The distribution of Ti and O elements overlaps almost completely, but the Ti element is more densely distributed, indirectly indicating the uniformly formation of TiO_2 on the MXene nanosheets [41, 42].

In addition, Figs. 2(f) and 2(g) present HRTEM images, demonstrating the interconnected structure of $Ti_3C_2T_x$ MXene, TiO_2, and CF. As illustrated in Fig. 2(e), the synthesized TiO_2 exhibits smooth and rounded edges, resembling a thin-sheet morphology. In Fig. 2(f), HRTEM reveals distinct lattice fringes with spacings of 0.23 and 0.24 nm, corresponding to the (103) crystal plane of $Ti_3C_2T_x$ and the (101) crystal plane of TiO_2, respectively [43]. Upon magnification of the HRTEM image in Fig. 2(g), numerous lattice defects are evident, including the disappearance of lattice fringes and point defects. As depicted, the yellow regions indicate the absence of lattice fringes, the white lines represent crystal planes, and the red circles highlight point defects. Similarly, Fig. S5 in the ESM also displays prominent lattice fringes corresponding to the (002) crystal plane of C, where the yellow areas signify the disappearance of lattice fringes due to lattice distortion, and the red lines designate the crystal planes. As can be seen from the TEM in Fig. 2(f), an N-doped amorphous structure is present in the crystal structure of $Ti_3C_2T_x$, which can generate many heterogeneous interfaces and is beneficial for interface polarization [44]. Based on the doping of N element and the *in-situ* growth of TiO_2, the rough surface and uneven interface might be benefit for multiple reflection and scattering of electromagnetic waves [43]. Therefore, the ingenious construction of a porous framework and the design of heterostructure engineering design are expected to have a positive impact on the absorption of electromagnetic waves [12].

The crystallinity can be calculated using the Debeye–Scherrer equation (Eq. (1)):

$$D = \frac{k\lambda}{\beta \cos\theta} \quad (1)$$

The crystallinity of the four different ratios of aerogels was calculated using JADE, as shown in Fig. S6 in the ESM. The crystallinity of these aerogels ranged between 30% and 45%, indicating good crystallinity. The XRD patterns of N-CMT nano-aerogels with different MXene contents and pure CF aerogel are presented in Fig. 3(a). Notably, characteristic peaks corresponding to the (002) and (006) planes of $Ti_3C_2T_x$ are observed at 7.1° and 18.1°, respectively, confirming the successful synthesis of MXene $Ti_3C_2T_x$ [45]. After thermal annealing at 700 °C, the peaks appeared at 27.8°, 36.1°, 41.3°, 43.7°, and 63.1° correspond to the (110), (101), (111), (210), and (002) planes of rutile-TiO_2 (PDF #21-1276), respectively. Meanwhile, other peaks located at 38.2°, 48.3°, 54.3°, and 55.3° are attributed to the (004), (200), (105), and (211) planes of anatase-TiO_2 (PDF #73-1764). This indicates that a portion of MXene $Ti_3C_2T_x$ is oxidized into TiO_2 after thermal annealing at 700 °C. Besides, the XRD diffraction spectrum of bio-degreased cotton balls after high-temperature carbonization under N_2 at 700 °C is provided. The broad peak between 20° and 30° is attributed to the carbonization of cotton into amorphous carbon, while the distinct diffraction peak at 2θ = 25.3° corresponds to the (002) plane of graphite [46, 47].

The results demonstrate that N-doped CF/MXene/TiO_2 nano-aerogel was successfully prepared. To further investigate the degree of graphitization of the N-CMT nano-aerogel, Raman spectroscopy was employed to analyze the crystalline structure and defect level of the cotton and the N-CMT 30% sample. As shown in Fig. S7 in the ESM, the D-band peak at 1350 cm^{-1} signifies disordered carbon vibrations and structural defects, while the G-band peak at

1600 cm^{-1} is associated with the degree of graphitization of carbon. The degree of graphitization can be expressed by the intensity ratio of the D-band to the G-band (I_D/I_G), where a lower I_D/I_G ratio indicates fewer carbon defects and a higher degree of graphitization. The I_D/I_G ratios for cotton and N-CMT 30% were 0.87 and 0.99, respectively, indicating high degrees of graphitization. Consequently, the diffraction peak observed at 2θ = 25.7° is correlated with the (002) plane of graphitic carbon and corresponds to the lattice spacing of 0.34 nm observed in TEM, suggesting that both the cotton and 3D N-CMT nano-aerogels exhibit good graphitic structures after thermal annealing.

To further delve into the surface chemical composition and elemental states of the N-CMT 30% aerogel composite material, measurements were conducted utilizing X-ray photoelectron spectroscopy (XPS), offering an insightful examination of its compositional and elemental characteristics (Figs. 3(b)–3(f). The XPS spectrum of the 3D N-CMT nano-aerogel indicates its main components are C, Ti, N, O, and F elements, consistent with the composition of MXene. As shown in Fig. 3(b), the peaks in the XPS spectrum belong to C 1s, Ti 2p, N 1s, and O 1s, respectively, and a residual peak belonging to F 1s is observed at 669.08 eV. In Fig. 3(c), the C 1s peaks detected at 288.03, 285.38, 284.28, 283.33, and 281.83 eV correspond to O=C–O, C–O, C–N, C–C/C=C, and Ti–C bonds, respectively [48]. The high-resolution Ti 2p spectrum in Fig. 3(d) is fitted into two pairs of 2p 1/2–2p 3/2 double peaks, corresponding to the Ti–C 、 Ti^{2+} and Ti–O bands. The absence of the Ti–Al band, along with the intensified Ti–C and Ti–O bands, indicates the successful etching of the Al atomic layer and its substitution by –OH and –O terminations. Furthermore, as illustrated in Fig. 3(e), the O 1s spectrum can be deconvoluted into distinct bands:

Ti–O at 529.73 eV, O–C–$(OH)_x$ at 532.83 eV, C–Ti–O_x at 531.13 eV, and C–Ti–$(OH)_x$ at 532.48 eV. The C–Ti–O_x and C–Ti–$(OH)_x$ bands are indicative of prevalent surface terminations, whereas the Ti–O band is attributed to the oxidation of $Ti_3C_2T_x$ [49–51]. Observing the N 1s spectrum in Fig. 3(f), it can be fitted into three main peaks. The main peak at 401.48 eV is attributed to quaternary N, indicating that the nitrogen in the composite material is primarily in the form of quaternary ammonium nitrogen [20]. This result aligns with previous reports on the pyrolysis of aromatic PI, which suggest that as the pyrolysis temperature increases, more quaternary nitrogen is incorporated into the carbon framework [21]. The presence of pyrrolic N at 400.53 eV indicates that carbon and nitrogen atoms are bonded in the form of –C–N–C– [20]. Quaternary N and pyrrolic N indicate that some nitrogen combines with carbon to form C–N bonds (quaternary N and pyrrolic N) within the lattice of $Ti_3C_2T_x$, while the remaining nitrogen replaces carbon to form Ti–N bonds [45]. The presence of the Ti–N peak indicates that nitrogen-doped N-$Ti_3C_2T_x$ was obtained during the thermal annealing process of the sample under a nitrogen atmosphere. The N-doped $Ti_3C_2T_x$ still maintains its accordion-like structure, along with additional micropores, incorporated N atoms, expanded interlayer spacing, and even the emergence of a new TiN phase [45]. These structural characteristics can provide polarization centers to facilitate dielectric loss. The above results further demonstrate the successful preparation of N-doped CF/MXene/TiO_2 nano-aerogel.

To understand the thermal stability of the material, the thermochemical processes of pure cotton and N-CMT 30% 3D nano-aerogel were investigated using a thermogravimetric analyzer, and the corresponding thermogravimetric analysis (TGA) curves were presented (Fig. S8 in the ESM). Between 100–340 °C, the 3D N-CMT nano-aerogel exhibited a faster mass loss compared to pure cotton, which was attributed to the loss of surface functional groups on the MXene component [52]. For pure cotton, the carbonization stage of thermal decomposition primarily involved

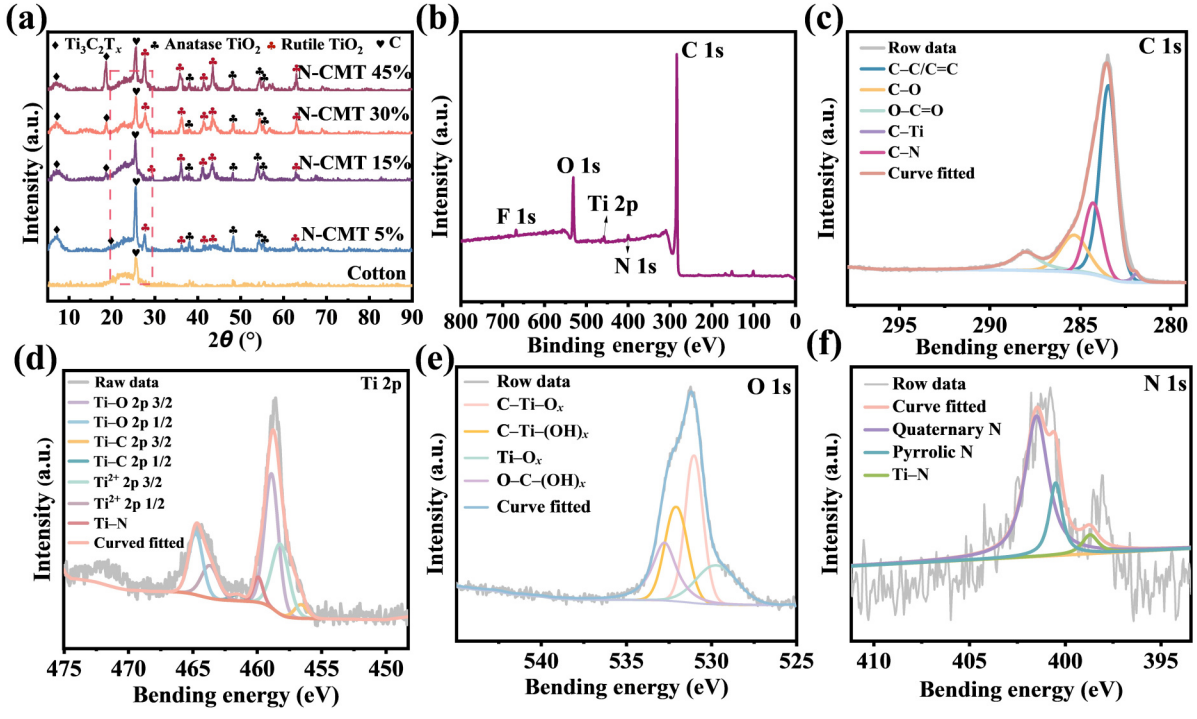


Figure 3 (a) XRD patterns of N-CMT nano-aerogels with different MXene contents and pure CF aerogel, (b)–(f) XPS survey spectrum and high-resolution spectra of C 1s, Ti 2p, O 1s, and N 1s for the N-CMT 30% nano-aerogel.

the removal of non-carbon light elements, random breakage of molecular chains, and continuous structural reorganization of carbon elements, ensuring the stability of the carbon framework. Prior to 650 °C, both the 3D N-CMT 30% nano-aerogel and pure cotton displayed similar thermal decomposition processes. By 800 °C, the mass loss of N-CMT 30% was only 13.7%, indicating its excellent thermal stability.

3.2 Electromagnetic parameters and microwave absorption performance

The evaluation metrics for electromagnetic wave absorption performance are typically represented by the minimum reflection loss (RL_{min}) and the EAB. To conduct a visual comparison of the EMA characteristics exhibited by different composites, Fig. 4 investigates the reflection loss (RL values and effective absorption bandwidths of all samples as functions of thickness and frequency. The RL values for different proportions of 3D N-CMT nano-aerogels are calculated using Eqs. (2) and (3) [15]

$$RL = 20\lg\left|\frac{Z_{in}-Z_0}{Z_{in}+Z_0}\right| \quad (2)$$

$$Z_{in} = Z_0(\mu_r/\varepsilon_r)^{1/2}\tanh\left[j(2\pi fd/c)(\mu_r\varepsilon_r)^{1/2}\right] \quad (3)$$

where, Z_{in} in represents the input impedance on the surface of the absorber, while Z_0 refers to the impedance of air. f denotes the microwave frequency, t represents the thickness of the absorber, and c is the speed of light in vacuum. The bandwidth where RL is less than −10 dB is defined as the effective absorption bandwidth. As can be seen from Figs. 4(a_1)–4(d_1), 3D N-CMT nano-aerogels with various MXene contents all exhibit excellent EMA performance. Additionally, the EMW electromagnetic performance of pure absorbent cotton and MXene is shown in the Fig. S9 in the ESM. The existence of the carbon fiber skeleton enhances multiple reflections and scattering of electromagnetic waves within the composites, and augments the contact area between various components, thereby establishing sufficient conductive channels within the composite aerogel. For the N-CMT 5% aerogel, the RL_{min} reaches −66.79 dB at a matching thickness of 2.36 mm (at 12.6 GHz), and the EAB achieves 5.26 GHz at 3 mm. For N-CMT15% aerogel, the lowest reflection loss value reaches −60.9 dB at a thickness of 3.5 mm, and the EAB reaches 7.38 GHz at a matching thickness of 3.2 mm. In the case of N-CMT 30% aerogel, the RL_{min} attains −72.56 dB and the EAB reaches 6.9 GHz at 2.23 mm. Specifically, when the thickness is adjusted from 1 mm to 5 mm, the effective absorption bandwidth of the N-CMT 30% aerogel reaches 13.94 GHz, achieving a coverage of 98% of the C-band and the entire X and Ku bands, accounting for 87% of the entire frequency range.

It is noteworthy that as the proportion of MXene further increases, the N-CMT 45% aerogel exhibits relatively poorer microwave absorption capabilities, with an RL_{min} value of only −21.04 dB at 3.06 mm. Therefore, it can be concluded that the ratio of MXene and TiO_2 particles in 3D N-CMT nano-aerogels plays a pivotal role in regulating the electromagnetic properties of the synthesized composite.

In addition, to achieve optimal electromagnetic wave absorption in practical applications, it is necessary to match the thickness of the absorber with the frequency. Typically, the RL_{min} of the samples and their thickness conform to the quarter-wavelength model, with the RL_{min} shifting towards lower frequencies as the thickness increases (Eq. (4)) [53, 54]:

$$t_m = \frac{n\lambda}{4} = \frac{nc}{4f_m\sqrt{|\mu_r||\varepsilon_r|}} \quad n = 1,3,5 \quad (4)$$

Here, f_m represents the frequency corresponding to the minimum reflection loss value, and t_m denotes the matching thickness of the sample. The purple solid line represents the theoretical matching thickness (d_m), while the blue hearts indicate the actual matching thickness. The simulation results agree well with the experimental data, indicating that interference cancellation plays a significant role in electromagnetic wave dissipation [55, 56].

For a deeper analysis of the absorption characteristics of the samples, impedance matching of 3D N-CMT nano-aerogels with different proportions was investigated. The impedance matching characteristic reflects the relationship between the input impedance and the impedance of free space, which can be evaluated by $Z = |Z_{in}/Z_0|$ [57]. When Z in is equal to or close to Z_0, it indicates that more EMW energy can enter the absorber, with almost zero reflection from the surface. Alternatively, in the case of impedance mismatch, most of the incident electromagnetic waves will be reflected and unable to enter the absorber. In such a scenario, even if the absorbers possess high dielectric capacity, they cannot exhibit good EMW absorption performance [58]. Therefore, impedance matching plays a crucial role in influencing the electromagnetic wave absorption capability [59].

The calculated Z-values for all samples are depicted in Figs. 4(a_4)–4(d_4). As can be observed from Figs. 4(a_4)–4(c_4), N-CMT 5%, N-CMT 15%, and N-CMT 30% aerogels all exhibit good impedance matching. However, due to the excessive content of MXene in N-CMT 45%, impedance mismatch occurs, resulting in most microwaves being reflected instead of penetrating into the interior (Fig. 4(d_4)) [40]. Generally, the primary electromagnetic energy conversion processes in absorbers involve capturing electromagnetic waves and converting them into heat and other forms of energy. The effectiveness of microwave penetration into the absorbing material is assessed by impedance matching. Meanwhile, the attenuation constant α signifies the capacity to reduce electromagnetic energy, which is obtained from the subsequent formula [63, 64]:

$$\alpha = \frac{\sqrt{2}\pi f}{c} + \sqrt{(\mu''\varepsilon'' - \mu'\varepsilon') + \sqrt{(\mu''\varepsilon'' - \mu'\varepsilon') + (\mu''\varepsilon'' - \mu'\varepsilon')}} \quad (5)$$

The superior microwave absorption performance of N-CMT nano-aerogels is primarily attributed to their strong electromagnetic wave attenuation capability and excellent impedance matching. Generally, numerous factors influence the attenuation constant (λ), and different loss mechanisms have distinct effects on its value. As shown in Fig. 5(d), the α value of the N-CMT 30% aerogel is the highest among the four aerogels, demonstrating its strongest attenuation ability for dissipating electromagnetic (EM) energy [65]. The introduction of CF into N-CMT nano-aerogels results in the formation of heterogeneous structures with high porosity and conductive networks, which facilitates the movement of carriers and charges within the MXene nanosheets. Additionally, it is evident that the *in-situ* generation of TiO_2 nanoparticles on the $Ti_3C_2T_x$ surface and the incorporation of nitrogen elements enhance the dielectric properties of MXene. Furthermore, the

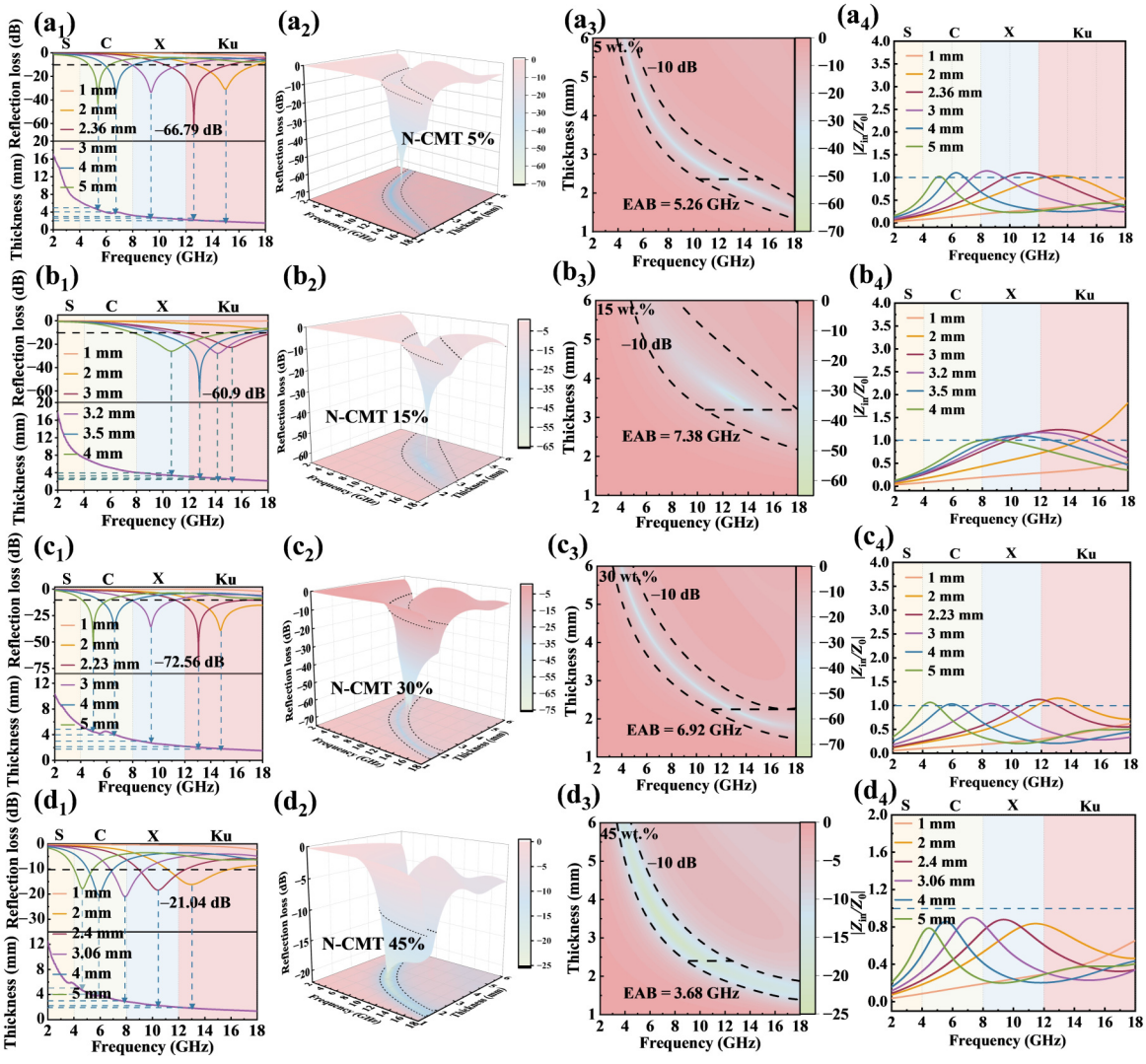


Figure 4 Reflection loss, 2D/3D contour images, and impedance images of (a_1)–(a_4) N-CMT 5% aerogel, (b_1)–(b_4) N-CMT 15% aerogel, (c_1)–(c_4) N-CMT 30% aerogel, (d_1)–(d_4) N-CMT 45% aerogel.

introduction of CF significantly affects the formation of conductive pathways, coupling with the multilayer structure of the $Ti_3C_2T_x/TiO_2$ samples, leading to multiple attenuations of electromagnetic waves. Consequently, the electromagnetic wave absorption performance of the N-doped CF/MXene/TiO_2 aerogel is significantly improved [38].

To further investigate the electromagnetic wave absorption mechanism of N-CMT nano-aerogels, electromagnetic parameters were tested for 3D N-CMT nano-aerogels with different MXene ratios. Figure 5(a) and 5(b) display the curves of the complex permittivity ($\varepsilon_r = \varepsilon' - j\varepsilon''$) for the four samples over the frequency range of 2–18 GHz. The real part ε' denotes the storage capacity of electromagnetic energy, while the imaginary part ε'' denotes the attenuation capacity of electromagnetic energy. Due to the nitridation treatment and thermal annealing of $Ti_3C_2T_x$ causing a certain degree of magnetic loss within the 2–18 GHz, as indicated in Figs. S10(a)–S10(c) in the ESM, the permeability parameters of the 3D N-CMT nano-aerogel exhibit fluctuations at low frequencies, which can be attributed to the occurrence of natural resonance in the sample [60]. As evident from Fig. S10(d) in the ESM, $\mu''(\mu')^{-1}f^{-1}$ remains constant within the 4–18 GHz, signifying that eddy current loss is dominant. Therefore, natural resonance loss and eddy current loss occur within the 2–4 GHz range (S-band), whereas only eddy current loss is present in the 4–18 GHz range. As shown in Fig. 5(a), the real part of the dielectric constant of 3D N-CMT nano-aerogels with different ratios exhibits a frequency-dependent behavior, gradually decreasing from low to high frequencies with minute fluctuations. This may be attributed to polarization phenomena and relaxation behaviors occurring within testing frequency range [61, 62]. Specifically, for N-CMT 5%, N-CMT 15%, N-CMT 30%, and N-CMT 45%, the values of ε' decrease from 9.75 to 6.99, 7.18 to 2.93, 9.8 to 5.15, and 12.18 to 5.43, respectively. As shown in Fig. 5(c), fluctuations can be observed at 2.64, 6.46, and 10.04 GHz for N-CMT 5%, and near 5.46, 10, and 12.76 GHz for N-CMT 30%, indicating the presence of polarization phenomena. The frequency bands and trends of fluctuations in the imaginary part of the dielectric constant for the four nano-aerogels with different proportions are distinct, primarily due to differences in their polarization forms. For N-CMT 5%, where the content of MXene is relatively low compared to that of

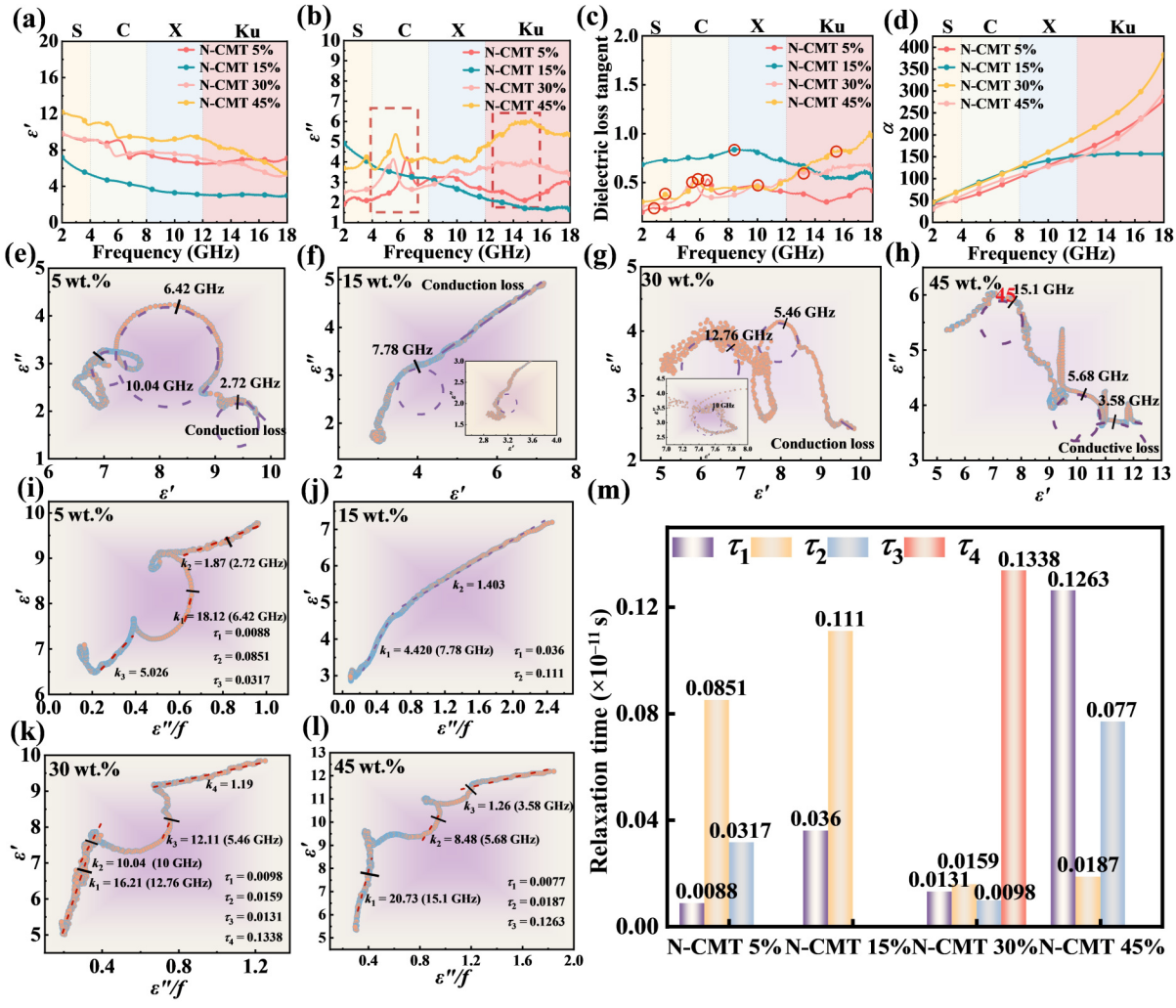


Figure 5 (a) Real part, (b) imaginary part, (c) dielectric loss tangent, (d) attenuation constant, and (e)–(h) Cole–Cole curves of 3D N-CMT nano-aerogels with varying MXene contents. (i)–(l) The relationships between ε' and ε''/f values for N-CMT5%, N-CMT15%, N-CMT 30%, and N-CMT45% aerogels. (m) A statistical overview of the relaxation times for all samples.

PI, a higher amount of nitrogen is provided after carbonization due to its greater relative content. This results in a higher concentration of nitrogen doping. The polarization is primarily attributed to defect-induced polarization, conduction loss, and interfacial polarization. In the case of N-CMT 15%, which has a lower MXene content and lower nitrogen doping concentration, conduction loss, interfacial polarization, and dipolar polarization are the primary loss mechanisms. The imaginary part of the dielectric constant (ε'') for N-CMT 15% exhibits a decreasing trend with increasing frequency, which may also be associated with dipolar polarization. Under the influence of an external electromagnetic field, dipoles rearrange; if these rearranged dipoles do not match the increasing frequency, the dipole-induced dielectric polarization effect weakens, resulting in a dielectric response that decreases with frequency. For N-CMT 30% and N-CMT 45%, with higher MXene contents and more polar functional groups on the MXene surface, the dielectric resonance peaks appearing in the 4–8 GHz range are attributed to the dipolar contributions after nitrogen doping, with the combined effects of dipolar polarization, interfacial polarization, and defect-induced polarization [63]. Compared to N-CMT 45%, the dielectric resonance peak for N-CMT 30% shifts slightly towards lower frequencies [59], and the fluctuation at 15 GHz represents a relaxation polarization trend at high frequencies, primarily relying on the abundant functional groups on the MXene surface acting as electric dipoles to provide dipolar polarization, further enhancing their attenuation capabilities [65].

Figure 5(c) shows the curves of the dielectric loss tangent values for the four proportions of aerogels within the 2–18 GHz range. Similarly, similar to the imaginary part of the permittivity curves, several dielectric loss peaks resulting from dielectric polarization can be observed. This is because when dipoles cannot respond to the changing electromagnetic field, corresponding hysteresis occurs in some specific frequency bands, and the dielectric loss peaks represent the relaxation process of dielectric polarization. According to the Debye model, when the electromagnetic field changes, polarization relaxation converts dielectric energy into thermal fluctuations, and the Cole–Cole plot can help determine whether the Debye relaxation process occurs.

According to the Debye relaxation equation, the real and imaginary parts of the permittivity can be obtained from the equations (Eqs. (6) and (7)):

$$\varepsilon' = \varepsilon_\infty + \frac{\varepsilon_s - \varepsilon_\infty}{1 + \omega^2\tau^2} \quad (6)$$

$$\varepsilon'' = \frac{\omega\tau(\varepsilon_s - \varepsilon_\infty)}{1+\omega^2\tau^2} \quad (7)$$

In this context, ε_s and ε_∞ represent the static permittivity and the permittivity at infinite frequency, respectively; ω and τ denote the angular frequency and relaxation time, respectively.

To better understand the polarization relaxation process during electromagnetic wave attenuation, the relaxation process was analyzed using Cole–Cole circles. Figures 5(e)–5(h) exhibits the Cole–Cole plots for N-CMT nano-aerogels with four different MXene proportions. The relationship between ε' and ε'' can be described as follows (Eq. (8)) [66]:

$$\left(\varepsilon' - \frac{\varepsilon_s + \varepsilon_\infty}{2}\right)^2 + (\varepsilon'')^2 = \left(\frac{\varepsilon_s - \varepsilon_\infty}{2}\right)^2 \quad (8)$$

The static dielectric constant at infinite frequency and the relative dielectric constant are represented by ε_s and ε_∞, respectively. The curves of ε' and ε'' exhibit individual cycles, with each cycle corresponding to a Debye relaxation process.

In the curves, ε' and ε'' exhibit their respective cycles, each corresponding to a Debye relaxation process. The relationship between ε' and ε'', as derived from the formula, should ideally form a semicircle. However, as observed in Figs. 5(e)–5(h), all samples exhibit a series of irregular, distorted semicircles. This is because 3D N-CMT nano-aerogels are multicomponent microwave absorbers, whereas the Debye equation is established under specific models. Inevitable defects and lattice distortions present in the aerogel samples lead to distortions in the semicircular shapes. Taking N-CMT 30% as an example, three peaks in its dielectric loss tangent ($\tan\delta_\varepsilon$) are observed at 5.56, 10.04, and 13.22 GHz (Fig. 5(c)), corresponding to three Debye relaxation processes at 5.46, 10, and 12.76 GHz (Fig. 5(g)). It is evident that some peaks in $\tan\delta_\varepsilon$ align with the corresponding frequencies of the Debye relaxation processes. Additionally, the other three samples exhibit similar characteristics. As can be observed from the Figs. 5(e)–5(h), the ε'–ε'' curves of 3D N-doped CF/MXene/TiO_2 nano-aerogels possess a series of distinct Debye relaxation processes, originating from the Debye relaxions of CF, MXene and TiO_2, as well as interfacial polarizations among them [67]. It is noteworthy that Fig. 5(g) presents multiple relaxation curves, indicative of the rich relaxation behavior in N-CMT 30% aerogel. The rich behavior can be ascribed to the functional groups on the surface of $Ti_3C_2T_x$ and TiO_2, as well as the dipole polarization caused by lattice defects resulting from nitrogen doping, and the interface polarization between the multi-component heterogeneous interfaces within the composites, leading to more Debye relaxation processes.

By rearranging Eqs. (6) and (7), the number of Debye relaxation processes and the corresponding Debye relaxation frequencies ($f_d = 1/\pi\tau$) can be roughly estimated as following Eq. (9):

$$\varepsilon' = \varepsilon_\infty + \frac{\varepsilon''}{\omega\tau} = \varepsilon_\infty + \frac{\varepsilon''}{2\pi f\tau} \quad (9)$$

From the aforementioned equations, it can be observed that during Debye relaxation, the connection between ε' and $\varepsilon'' f$ is represented by a straight line with a slope of $1/2\pi\tau$, enabling the calculation of the relaxation time τ for polarization relaxation. As shown in Figs. 5(i)–5(l), some curves are not entirely linear, which may be due to the influence of other mechanisms such as conductive losses. By comparing the frequencies corresponding to Debye relaxation and the frequencies of dielectric loss for samples of various proportions, based on Figs. 5(c) and 5(i)–5(l), as summarized in Table S3 in the ESM, it is evident that 3D N-CMT nano-aerogels exhibit dielectric polarization processes that conform to the Debye model. Therefore, considering the calculation errors and potential impacts of other mechanisms, it is relatively reasonable to establish a relationship between the peak frequencies and the corresponding polarization frequencies [68]. Figure 5(m) presents a summary of the relaxation times for samples of the four proportions. Evidently, all samples with different proportions exhibit distinct relaxation times, which can be attributed to the presence of various polarization relaxation processes within the composites. These different polarization relaxation processes contribute in distinct ways to the attenuation of electromagnetic waves [69]. In view of this phenomenon, polarization relaxation can be interpreted from two aspects including interfacial polarization and dipolar polarization. Interfacial polarization is caused by the accumulation of charges/holes at heterogeneous interfaces, particularly the heterogeneous interface formed between $Ti_3C_2T_x$ and TiO_2. While dipolar polarization arises from defects and functional groups on the surfaces of $Ti_3C_2T_x$ and TiO_2, as well as lattice defects caused by nitrogen doping. Nitrogen doping can induce the formation of sp^3 defects and disordered sites in $Ti_3C_2T_x$, which enhances dipolar polarization relaxation, thereby regulating dielectric property and enhancing electromagnetic wave absorption performance. Additionally, at heterogeneous interfaces, the electrons accumulate and rearrange, generating an internal electric field that opposes the external electric field, thereby reducing a portion of the electromagnetic energy.

As shown in Fig. 6(d), N-CMT 5%, N-CMT 15%, and N-CMT 30% all exhibited excellent electromagnetic wave absorption properties. To further validate this conclusion, Figs. 6(a)–6(c) illustrates the relationships between impedance matching ratio, attenuation constant, and the RL_{min} for N-CMT 5%, N-CMT 15%, and N-CMT 30% [40]. N-CMT 30% aerogel demonstrated the lowest RL_{min} and possessed the largest attenuation constant. When comparing the impedance matching of the three aerogel compositions, it was observed that all three aerogels exhibited optimal impedance matching when the value of $|Z_{in}/Z_0|$ approached 1, leading to minimized reflection losses. Notably, N-CMT 30% exhibited the best impedance matching and strongest attenuation capabilities across the entire frequency range, achieving optimal microwave absorption performance. We compared the microwave absorption performance of MXene-based composites published on Web of Science in recent years, as presented in Figs. 6(e) and 6(f) and the specific information is shown in Table S4 in the ESM. 3D N-CMT nano-aerogel was synthesized by vacuum impregnation of biomass-based absorbent cotton balls and the in-situ generation of TiO_2 nanospheres on MXene to adjust the density of the cross-linked network and optimize the conductive network. Additionally, the presence of multiple heterogeneous interfaces enhances EMA performance. Compared to other MXene-based or MXene/TiO_2-based materials, in the aspects of RL_{min} and EAB, the three N-CMT nano-aerogels achieved excellent RL_{min} values and EAB performance at thinner thicknesses. This suggests that the prepared materials can be considered attractive candidates as electromagnetic wave absorbers.

Based on the aforementioned analysis, two crucial factors need to be taken into account in the micro-macro interface engineering design of 3D N-CMT nano-aerogel materials including impedance matching and electromagnetic wave loss within the absorber.

From a macroscopic structural perspective, the introduction of a

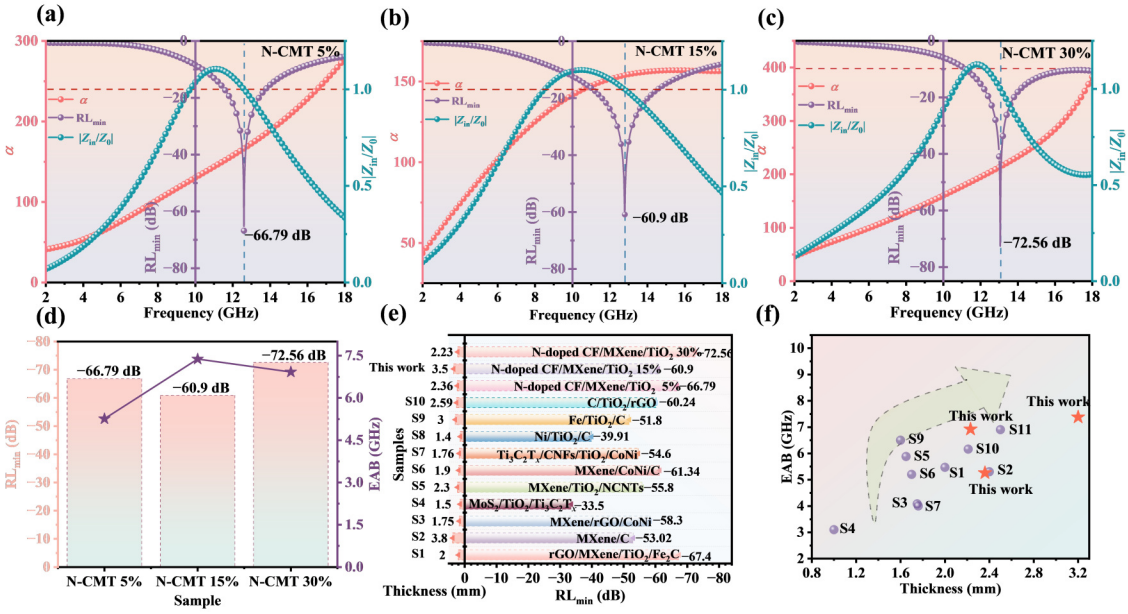


Figure 6 (a)–(c) RL_{min}, $|Z_{in}/Z_0|$, and α values of N-CMT 5%, N-CMT 15%, and N-CMT 30% aerogels at their optimal thicknesses under different frequencies. (d) RL_{min} and EAB values of N-CMT 5%, N-CMT 15%, and N-CMT 30% aerogels at the most suitable thickness. (e) and (f) Comparison of the microwave absorption performance between 3D N-CMT nano-aerogels and MXene-based microwave absorbing materials published on Web of Science in recent years

carbon fiber framework enlarges the interlayer spacing of N-CMT nano-aerogels compared to $Ti_3C_2T_x$ MXene multilayer films with narrower etched interlayer distances. This enlargement enables the introduction of abundant void spaces between adjacent $Ti_3C_2T_x$ nanosheet layers. And due to the carbonization of aromatic PI, carbon microcrystals are formed, introducing a large number of micropores into the matrix [70]. Additionally, the construction of a continuous hierarchical structure facilitates multiple reflections and scatterings of incident electromagnetic waves, extending their transmission paths and enhancing electromagnetic energy dissipation. Furthermore, the hierarchical structure with expanded interlayer spacing and void spaces serves as an effective impedance matching medium, balancing the dielectric impedance between the N-CMT nano-aerogel and air.

From a microscopic perspective, dielectric loss is caused by the lag effect of dielectric conductivity and dielectric polarization. The dielectric loss capacity dominates the electromagnetic energy conversion process, encompassing conduction loss, dipolar polarization, defect-induced polarization, and interfacial polarization [71].

(1) Electron migration mainly originates from the conductive network composed of $Ti_3C_2T_x$ MXene layers, and CF. TiO_2 microspheres can also effectively adjust the density of the cross-linked network to optimize conduction loss. Due to the introduction of functional groups and nitrogen atoms on the surface of $Ti_3C_2T_x$, lattice distortion is caused, leading to the formation of point defects and dipoles, which result in polarization loss [72]. Moreover, the presence of TiO_2 on the $Ti_3C_2T_x$ layers results in uneven charge distribution on the interface due to differences in conductivity, which can be equivalent to a capacitor model as shown in Fig. 7. TiO_2 nanoparticles, with nanometer-scale sizes, have increased defects, dipoles, and dangling bonds compared to pure MXene. Furthermore, their oxygen defects can induce charge carriers such as holes or electrons, blocking electron transmission channels and disrupting the conservation of charge distribution.

Additionally, the unit polarization strategy indicates that lattice polarization caused by changes in the volume of titanium dioxide unit cells can effectively influence dielectric loss capabilities, enhancing conductive loss and polarization relaxation [57]. *In-situ* derived TiO_2 can be embedded into MXene to form Schottky contacts, and the built-in electric field in the Schottky barrier facilitates the loss of electromagnetic waves [24].

(2) Due to the significant difference in electrical conductivity between MXene and TiO_2, electrons accumulate at the interface between MXene nanosheets and TiO_2. Some electrons cannot keep up with the alternating electromagnetic field, and under an external electric field, charges undergo local motion, resulting in changes in dipole moments. When the frequency of charge changes cannot match the changes in the external frequency, polarization relaxation occurs, as shown in Fig. 7. Since the size of TiO_2 nanoparticles is small enough, more interactions occur between TiO_2 and the host structure, leading to Maxwell-Wagner-Sillars polarization [73]. Meanwhile, the addition of CF increases the surface area of the three-dimensional structure, and a larger surface area results in a greater possibility of interface polarization [64].

Furthermore, the nitridation treatment and thermal annealing of $Ti_3C_2T_x$ can induce a certain level of magnetic loss, and when acting in conjunction with natural resonance and eddy current loss, it may further enhance its impedance matching and microwave absorption (MA) characteristics.

In summary, due to the connections of CF and the synergistic effects generated by $Ti_3C_2T_x$ and TiO_2 on the surface, the N-doped CF/MXene/TiO_2 composite nano-aerogel exhibits excellent electromagnetic wave absorption properties.

To evaluate the electromagnetic absorption (EMA) performance of N-CMT nano-aerogels in practical applications, CST Studio Suite to calculate the radar cross-section (RCS) values of pure PEC plates and PEC plates coated with various 3D N-CMT nano-aerogels were explored, as shown in Figs. 8(a)–8(e) and Fig. S11 in the ESM [72]. Figure 8(f) displays the RCS curves of the PEC board and the N-CMT nanogel-coated PEC board across a scattering

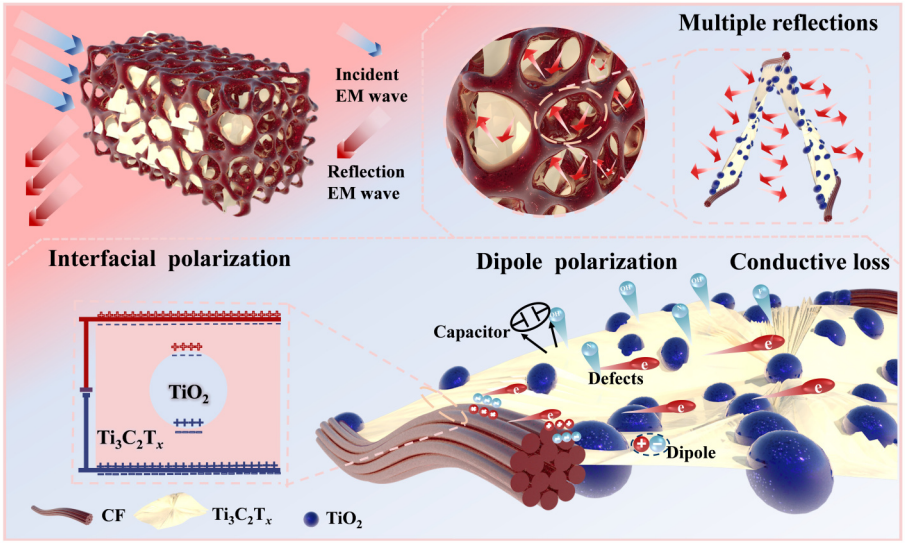


Figure 7 Schematic diagram of the electromagnetic wave absorption mechanism of 3D N-CMT nano aerogel.

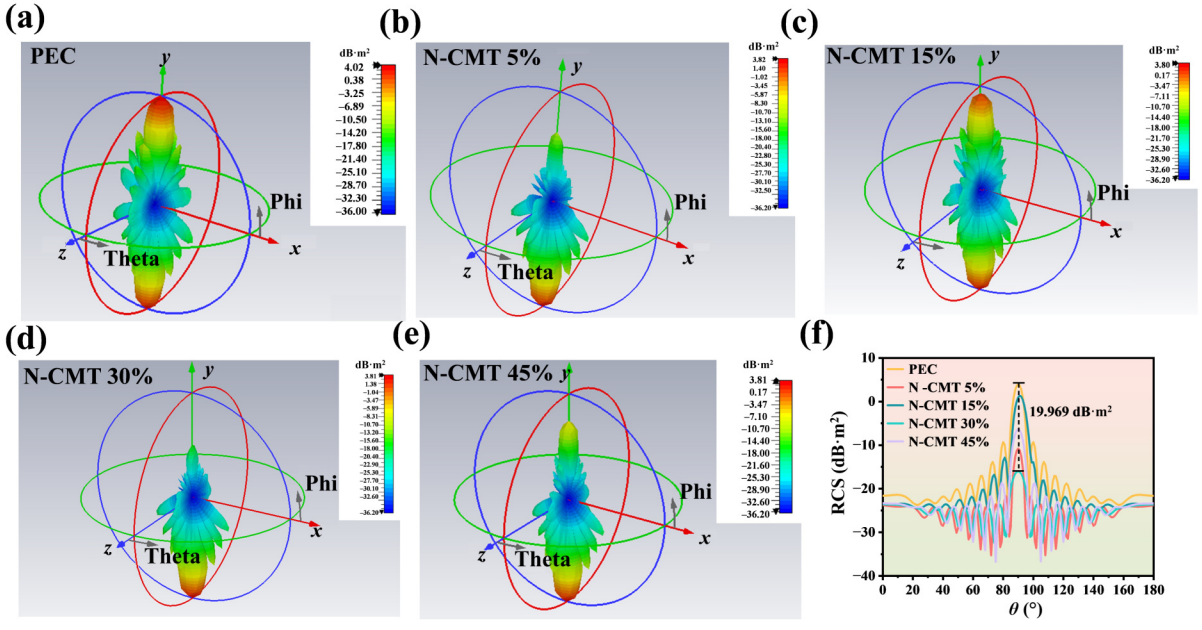


Figure 8 (a)–(e) CST simulation results for pure PEC plate and PEC plates coated with N-CMT5%, N-CMT15%, N-CMT 30%, and N-CMT45%. (f) Simulated RCS reduction values for PEC and N-CMT nano-aerogel-coated PEC plates at scattering angles ranging from 0° to 180°.

angle range of 0° to 180° at 12.6 GHz. The PEC board exhibited the highest radar scattering intensity, whereas the RCS of the N-CMT nanogel-coated PEC board was significantly reduced compared to the pristine PEC board. Additionally, RCS values at 13.06 GHz (Figs. S12 and S13 in the ESM) and 13.56 GHz (Fig. S14 in the ESM) were simulated, demonstrating that rational heterogeneous structural design can effectively reduce RCS values. Figure S15 in the ESM presents a comparative bar graph of RCS reduction values at different angles across three distinct frequencies. It was observed that at 12.6 GHz, with Theta at 90°, the maximum RCS reduction of the N-CMT 30% sample reached 19.969 dB·m^2. These results indicate that 3D N doped-CF/MXene/TiO_2 nano-aerogels possess promising applications as lightweight EMA coatings [75].

4 Conclusion

In summary, based on micro-macro interface engineering design strategy, 3D N-CF/MXene/TiO_2 nano-aerogels were successfully prepared combining vacuum impregnation and freeze-drying methods. The introduction of cotton derived CF allowed electromagnetic waves to undergo multiple reflection and scattering within the porous framework. *In-situ* generated TiO_2 on $Ti_3C_2T_x$ MXene nanosheets and the doping of nitrogen atoms effectively modulate the conductivity and create abundant heterogeneous interfaces. Apparently, due to the connections of CF, as well as the synergistic effects generated by $Ti_3C_2T_x$ and TiO_2 on the surface, 3D N-CMT nano-aerogels exhibited excellent EMA properties. For N-CMT 15%, an RL_{min} of −60.9 dB was achieved at a thickness of 3.5 mm, with an EAB of 7.38 GHz at 3.2 mm. Remarkably, N-CMT 30% achieved an RL_{min} of −72.56 dB and an EAB of 6.92 GHz at 2.23 mm. Furthermore, RCS simulation results demonstrated that the RCS reduction value of N-CMT 30% aerogel could reach 19.969 dB^2. Therefore, the proposed 3D N-CMT nano-aerogels with

ingenious heterogeneous interface engineering design have demonstrated tremendous potential in electromagnetic protection and stealth technology fields, providing a critical reference for the efficient absorbers in the future.

Electronic Supplementary Material: Supplementary material (sample density, stress–strain curve, nitrogen adsorption curve, pore size distribution curve, transmission curve, crystallinity, Raman spectrum, HRTEM images, and electromagnetic performance curve of the pure sample, etc.) is available in the online version of this article at https://doi.org/10.26599/NR.2025.94907169.

Data availability

All data needed to support the conclusions in the paper are presented in the manuscript and the ESM. Additional data related to this paper may be requested from the corresponding author upon request.

Acknowledgements

This work was supported by Joint Funds of the National Natural Science Foundation of China (Nos. U22A20244, U23A20673 and 52478261), Qingchuang Technology Project under Grant 2021KJ045, Demonstration Project of Benefiting People with Science and Technology of Qingdao, China (No. 24-1-8-cspz-9-nsh), and the China Postdoctoral Science Foundation (No. 2024M750580).

Declaration of competing interest

All the contributing authors report no conflict of interests in this work.

Author contribution statement

Y. L.: Conceptualization, experimental design, writing – review & editing, supervision, funding acquisition. C. L. D.: Writing – original draft, data curation, experimental design. S. J. W.: Investigation. D. Y. L.: Project administration, supervision, funding acquisition, resources. B. B. Y.: Supervision. Y. F. C.: Supervision. Y. R. W.: Supervision. R. L.: Supervision. All the authors have approved the final manuscript.

Use of AI statement

None.

References

[1] Liang, L. Y.; Li, Q. M.; Yan, X.; Feng, Y. Z.; Wang, Y. M.; Zhang, H. B.; Zhou, X. P.; Liu, C. T.; Shen, C. Y.; Xie, X. L. Multifunctional magnetic $Ti_3C_2T_x$ MXene/graphene aerogel with superior electromagnetic wave absorption performance. *ACS Nano* **2021**, *15*, 6622–6632.

[2] Deng, B. W.; Xiang, Z.; Xiong, J.; Liu, Z. C.; Yu, L. Z.; Lu, W. Sandwich-like Fe&TiO_2@C nanocomposites derived from MXene/Fe-MOFs hybrids for electromagnetic absorption. *Nano-Micro Lett.* **2020**, *12*, 55.

[3] Liu, J.; Zhang, H. B.; Xie, X.; Yang, R.; Liu, Z. S.; Liu, Y. F.; Yu, Z. Z. Multifunctional, superelastic, and lightweight MXene/polyimide aerogels. *Small* **2018**, *14*, 1802479.

[4] Wu, Y.; Tan, S. J.; Fang, G.; Zhang, Y. Q.; Ji, G. B. Manipulating CNT films with atomic precision for absorption effectiveness-enhanced electromagnetic interference shielding and adaptive infrared camouflage. *Adv. Funct. Mater.*, in press, DOI: 10.1002/adfm.202402193.

[5] Wang, Y. Q.; Zhao, H. B.; Cheng, J. B.; Liu, B. W.; Fu, Q.; Wang, Y. Z. Hierarchical $Ti_3C_2T_x$@ZnO hollow spheres with excellent microwave absorption inspired by the visual phenomenon of eyeless urchins. *Nano-Micro Lett.* **2022**, *14*, 76.

[6] Lyu, J.; Liu, Z. W.; Wu, X. H.; Li, G. Y.; Fang, D.; Zhang, X. T. Nanofibrous Kevlar aerogel films and their phase-change composites for highly efficient infrared stealth. *ACS Nano* **2019**, *13*, 2236–2245.

[7] Liu, C. Y.; Xu, L.; Xiang, X. Y.; Zhang, Y. J.; Zhou, L.; Ouyang, B.; Wu, F.; Kim, D. H.; Ji, G. B. Achieving ultra-broad microwave absorption bandwidth around millimeter-wave atmospheric window through an intentional manipulation on multi-magnetic resonance behavior. *Nano-Micro Lett.* **2024**, *16*, 176.

[8] Low, J.; Yu, J. G.; Jaroniec, M.; Wageh, S.; Al-Ghamdi, A. A. Heterojunction photocatalysts. *Adv. Mater.* **2017**, *29*, 1601694.

[9] Quan, B.; Liang, X. H.; Ji, G. B.; Cheng, Y.; Liu, W.; Ma, J. N.; Zhang, Y. N.; Li, D. R.; Xu, G. Y. Dielectric polarization in electromagnetic wave absorption: Review and perspective. *J. Alloys Compd.* **2017**, *728*, 1065–1075.

[10] Liang, H. S.; Chen, G.; Liu, D.; Li, Z. J.; Hui, S. C.; Yun, J. J.; Zhang, L. M.; Wu, H. J. Exploring the Ni 3*d* orbital unpaired electrons induced polarization loss based on Ni single-atoms model absorber. *Adv. Funct. Mater.* **2023**, *33*, 2370037.

[11] You, W. B.; Che, R. C. Excellent NiO–Ni nanoplate microwave absorber via pinning effect of antiferromagnetic-ferromagnetic interface. *ACS Appl. Mater. Interfaces* **2018**, *10*, 15104–15111.

[12] Pan, F.; Cai, L.; Shi, Y.; Dong, Y.; Zhu, X.; Cheng, J.; Jiang, H.; Wang, X.; Jiang, Y.; Lu, W. Heterointerface engineering ofβ-chitin/carbon nano-onions/Ni–P composites with boosted maxwell-wagner-sillars effect for highly efficient electromagnetic wave response and thermal management. *Nano-Micro Lett.* **2022**, *14*, 85.

[13] Shahzad, F.; Alhabeb, M.; Hatter, C. B.; Anasori, B.; Man Hong, S.; Koo, C. M.; Gogotsi, Y. Electromagnetic interference shielding with 2D transition metal carbides (MXenes). *Science* **2016**, *353*, 1137–1140.

[14] Liang, L. L.; Yang, X. Y.; Li, C.; Yu, R. L.; Zhang, B. S.; Yang, Y.; Ji, G. B. MXene-enabled pneumatic multiscale shape morphing for adaptive, programmable and multimodal radar-infrared compatible camouflage. *Adv. Mater.* **2024**, *36*, 2313939.

[15] Pan, F.; Wu, X. F.; Batalu, D.; Lu, W.; Guan, H. T. Assembling of low-dimensional aggregates with interlaminar electromagnetic synergy network for high-efficient microwave absorption. *Adv. Powder Mater.* **2023**, *2*, 100100.

[16] Shu, X. F.; Cheng, J.; Fang, B.; Wang, J. T.; Song, Y. N.; Lu, W.; Zhao, Z. J. Morphology-dependent magnetic role of ZIFs in nitrogen-doped MXene as metallic conductor microwave absorber. *Chem. Eng. J.* **2023**, *474*, 145817.

[17] Yang, C. H.; Tang, Y.; Tian, Y. P.; Luo, Y. Y.; Faraz Ud Din, M.; Yin, X. T.; Que, W. X. Flexible nitrogen-doped 2D titanium carbides (MXene) films constructed by an *ex situ* solvothermal method with extraordinary volumetric capacitance. *Adv. Energy Mater.* **2018**, *8*, 1802087.

[18] Pan, Z. H.; Ji, X. H. Facile synthesis of nitrogen and oxygen co-doped C@Ti_3C_2 MXene for high performance symmetric supercapacitors. *J. Power Sources* **2019**, *439*, 227068.

[19] Jiang, D.; Wei, M.; Du, X. J.; Qin, M.; Shan, X. L.; Chen, Z. D. One-pot synthesis of ZnO quantum dots/N-doped Ti_3C_2 MXene: Tunable nitrogen-doping properties and efficient electrochemiluminescence sensing. *Chem. Eng. J.* **2022**, *430*, 132771.

[20] Chen, Y.; Gao, Z.; Zhang, B.; Zhao, S. C.; Qin, Y. Graphene coated with controllable N-doped carbon layer by molecular layer deposition as electrode materials for supercapacitors. *J. Power Sources* **2016**, *315*, 254–260.

[21] Li, Y. Z.; Dong, J.; Zhang, J. X.; Zhao, X.; Yu, P. P.; Jin, L.; Zhang, Q. H. Nitrogen-doped carbon membrane derived from polyimide as free-standing electrodes for flexible supercapacitors. *Small* **2015**, *11*, 3476–3484.
[22] Machnikowski, J.; Grzyb, B.; Weber, J. V.; Frackowiak, E.; Rouzaud, J. N.; Béguin, F. Structural and electrochemical characterisation of nitrogen enriched carbons produced by the co-pyrolysis of coal-tar pitch with polyacrylonitrile. *Electrochim. Acta* **2004**, *49*, 423–432.
[23] Silva, R.; Voiry, D.; Chhowalla, M.; Asefa, T. Efficient metal-free electrocatalysts for oxygen reduction: Polyaniline-derived N- and O-doped mesoporous carbons. *J. Am. Chem. Soc.* **2013**, *135*, 7823–7826.
[24] Li, Y.; Luo, Z.; Yang, L.; Luo, Y. M.; Li, Q.; Zhang, L. Y.; Xiang, K. Influence of polyamide acid coating reaction on the properties of aramid fibre. *Polymer* **2019**, *178*, 121550.
[25] Chen, W. J.; Chen, W.; Zhang, B. Q.; Yang, S. Y.; Liu, C. Y. Thermal imidization process of polyimide film: Interplay between solvent evaporation and imidization. *Polymer* **2017**, *109*, 205–215.
[26] Zhang, Y. L.; Yan, Y.; Qiu, H.; Ma, Z. L.; Ruan, K. P.; Gu, J. W. A mini-review of MXene porous films: Preparation, mechanism and application. *J. Mater. Sci. Technol.* **2022**, *103*, 42–49.
[27] Sun, R. H.; Zhang, H. B.; Liu, J.; Xie, X.; Yang, R.; Li, Y.; Hong, S.; Yu, Z. Z. Highly conductive transition metal carbide/carbonitride(MXene)@polystyrene nanocomposites fabricated by electrostatic assembly for highly efficient electromagnetic interference shielding. *Adv. Funct. Mater.* **2017**, *27*, 1702807.
[28] Li, X. L.; Yin, X. W.; Song, C. Q.; Han, M. K.; Xu, H. L.; Duan, W. Y.; Cheng, L. F.; Zhang, L. T. Self-assembly core-shell graphene-bridged hollow MXenes spheres 3D foam with ultrahigh specific EM absorption performance. *Adv. Funct. Mater.* **2018**, *28*, 1803938.
[29] Guan, H. T.; Wang, Q. Y.; Wu, X. F.; Pang, J.; Jiang, Z. Y.; Chen, G.; Dong, C. J.; Wang, L. H.; Gong, C. H. Biomass derived porous carbon (BPC) and their composites as lightweight and efficient microwave absorption materials. *Compos. Part B: Eng.* **2021**, *207*, 108562.
[30] Wang, B. J.; Li, S. K.; Huang, F. Z.; Wang, S. P.; Zhang, H.; Liu, F. H.; Liu, Q. C. Construction of multiple electron transfer paths in 1D core-shell hetetrostructures with MXene as interlayer enabling efficient microwave absorption. *Carbon* **2022**, *187*, 56–66.
[31] Zhang, Z.; Zhao, H. Q.; Gu, W. H.; Yang, L. J.; Zhang, B. S. A biomass derived porous carbon for broadband and lightweight microwave absorption. *Sci. Rep.* **2019**, *9*, 18617.
[32] Li, Q. S.; Zhu, J. J.; Wang, S. N.; Huang, F.; Liu, Q. C.; Kong, X. K. Microwave absorption on a bare biomass derived holey silica-hybridized carbon absorbent. *Carbon* **2020**, *161*, 639–646.
[33] Zhao, H. Q.; Cheng, Y.; Zhang, Z.; Zhang, B. S.; Pei, C. C.; Fan, F. Y.; Ji, G. B. Biomass-derived graphene-like porous carbon nanosheets towards ultralight microwave absorption and excellent thermal infrared properties. *Carbon* **2021**, *173*, 501–511.
[34] Cao, Y. H.; Wang, K. L.; Wang, X. M.; Gu, Z. R.; Fan, Q. H.; Gibbons, W.; Hoefelmeyer, J. D.; Kharel, P. R.; Shrestha, M. Hierarchical porous activated carbon for supercapacitor derived from corn stalk core by potassium hydroxide activation. *Electrochim. Acta* **2016**, *212*, 839–847.
[35] Zhou, Y.; Zhou, W. J.; Ni, C. H.; Yan, S. G.; Yu, L. M.; Li, X. "Tree blossom" Ni/NC/C composites as high-efficiency microwave absorbents. *Chem. Eng. J.* **2022**, *430*, 132621.
[36] Liu, H. L.; Wang, P.; Zhang, B.; Li, H. Y.; Li, J.; Li, Y. J.; Chen, Z. Enhanced thermal shrinkage behavior of phenolic-derived carbon aerogel-reinforced by HNTs with superior compressive strength performance. *Ceram. Int.* **2021**, *47*, 6487–6495.
[37] Liang, X. C.; Liu, S. Y.; Zhong, S. J.; Zhang, S. T.; Meng, X. W.; Zhang, Y.; Yu, M. J.; Wang, C. G. A novel synthesis of Porous Fe_4N/carbon hollow microspheres for thin and efficient electromagnetic wave absorbers. *J. Colloid Interface Sc.* **2023**, *637*, 123–133.
[38] Shang, S. S.; Ye, X.; Jiang, X.; You, Q.; Zhong, Y.; Wu, X. D.; Cui, S. Preparation and characterization of cellulose/attapulgite composite aerogels with high strength and hydrophobicity. *J. Non-Cryst. Solids* **2021**, *569*, 120922.
[39] Xu, H. X.; Zhang, G. Z.; Wang, Y.; Ning, M. Q.; Ouyang, B.; Zhao, Y.; Huang, Y.; Liu, P. B. Size-dependent oxidation-induced phase engineering for MOFs derivatives via spatial confinement strategy toward enhanced microwave absorption. *Nano-Micro Lett.* **2022**, *14*, 102.
[40] Wang, Y.; Qu, Z. J.; Wang, W.; Qian, H. F.; Song, X. Y.; Yu, D. Multidimensional nanomaterials synergistic polyimide nanofiber/MXene/$NiFe_2O_4$ hybrid aerogel for high-performance microwave absorption. *Chem. Eng. J.* **2023**, *470*, 144435.
[41] Liu, N. N.; Yu, L. L.; Liu, B. J.; Yu, F.; Li, L. Q.; Xiao, Y.; Yang, J. H.; Ma, J. Ti_3C_2-MXene partially derived hierarchical 1D/2D TiO_2/Ti_3C_2 heterostructure electrode for high-performance capacitive deionization. *Adv. Sci.* **2023**, *10*, 2204041.
[42] Zhou, C. L.; Wang, X. X.; Luo, H.; Deng, L. W.; Wei, S.; Zheng, Y. W.; Jia, Q.; Liu, J. Q. Rapid and direct growth of bipyramid TiO_2 from $Ti_3C_2T_x$ MXene to prepare Ni/TiO_2/C heterogeneous composites for high-performance microwave absorption. *Chem. Eng. J.* **2020**, *383*, 123095.
[43] Gao, X. R.; Wang, B. B.; Wang, K. K.; Xu, S.; Liu, S. P.; Liu, X. H.; Jia, Z. R.; Wu, G. L. Design of $Ti_3C_2T_x/TiO_2$/PANI multi-layer composites for excellent electromagnetic wave absorption performance. *J. Colloid Interface Sci.* **2021**, *583*, 510–521.
[44] Li, R. K.; Lu, J. Q.; Li, C. J.; Cui, Y.; Lv, D. F.; Chen, Y. J.; Wei, Y. N.; Wei, H. Y.; Liang, B.; Bu, J. L. Mesoporous vanadium nitride nanofiber@N-doped carbon with excellent microwave absorption and anti-corrosion. *Colloids Surf. A: Physicochem. Eng. Aspects* **2024**, *686*, 133420.
[45] Yu, J. L.; Zeng, M. L.; Zhou, J.; Chen, H. D.; Cong, G. T.; Liu, H. C.; Ji, M. W.; Zhu, C. Z.; Xu, J. A one-pot synthesis of nitrogen doped porous MXene/TiO_2 heterogeneous film for high-performance flexible energy storage. *Chem. Eng. J.* **2021**, *426*, 130765.
[46] Wu, F. S.; Hu, P. Y.; Hu, F. Y.; Tian, Z. H.; Tang, J. W.; Zhang, P. G.; Pan, L.; Barsoum, M. W.; Cai, L. Z.; Sun, Z. M. Multifunctional MXene/C aerogels for enhanced microwave absorption and thermal insulation. *Nano-Micro Lett.* **2023**, *15*, 194.
[47] Fang, G.; He, T. A.; Hu, X. X.; Yang, X. M.; Zheng, S. Q.; Xu, G. Y.; Liu, C. Y. Bionic octopus structure Inspired Stress-Driven reconfigurable microwave absorption and multifunctional compatibility in infrared stealth and De-icing. *Chem. Eng. J.* **2023**, *467*, 143266.
[48] Li, X. Y.; Liu, S. Y.; Meng, X. W.; Zhang, S. T.; Yu, M. J.; Wu, L. F.; Liang, X. M. Modified antistatic carbonaceous fiber with excellent hydrophobicity, environmental stability and radar absorption performance. *Carbon* **2024**, *229*, 119501.
[49] Han, F.; Luo, S. J.; Xie, L. Y.; Zhu, J. J.; Wei, W.; Chen, X.; Liu, F. W.; Chen, W.; Zhao, J. L.; Dong, L. et al. Boosting the yield of MXene 2D sheets via a facile hydrothermal-assisted intercalation. *ACS Appl. Mater. Interfaces* **2019**, *11*, 8443–8452.
[50] Xing, C. Y.; Chen, S. Y.; Liang, X.; Liu, Q.; Qu, M. M.; Zou, Q. S.; Li, J. H.; Tan, H.; Liu, L. P.; Fan, D. Y. et al. Two-dimensional MXene (TiC)-integrated cellulose hydrogels: Toward smart three-dimensional network nanoplatforms exhibiting light-induced swelling and bimodal photothermal/chemotherapy anticancer activity. *ACS Appl. Mater. Interfaces* **2018**, *10*, 27631–27643.
[51] Yang, M. L.; Yuan, Y.; Li, Y.; Sun, X. X.; Wang, S. S.; Liang, L.; Ning, Y. H.; Li, J. J.; Yin, W. L.; Li, Y. B. Anisotropic electromagnetic absorption of aligned $Ti_3C_2T_x$ MXene/gelatin nanocomposite aerogels. *ACS Appl. Mater. Interfaces* **2020**, *12*, 33128–33138.
[52] Han, M. K.; Yin, X. W.; Wu, H.; Hou, Z. X.; Song, C. Q.; Li, X. L.; Zhang, L. T.; Cheng, L. F. Ti_3C_2 MXenes with modified surface for high-performance electromagnetic absorption and shielding in the X-band. *ACS Appl. Mater. Interfaces* **2016**, *8*, 21011–21019.
[53] Yang, K.; Cui, Y. H.; Wan, L. Y.; Wang, Y. B.; Tariq, M. R.; Liu, P.;

Zhang, Q. Y.; Zhang, B. L. Preparation of three-dimensional Mo_2C/NC@MXene and its efficient electromagnetic absorption properties. *ACS Appl. Mater. Interfaces* **2022**, *14*, 7109–7120.

[54] Cheng, Y. J.; Sun, X. X.; Yang, S.; Wang, D.; Liang, L.; Wang, S. S.; Ning, Y. H.; Yin, W. L.; Li, Y. B. Multifunctional elastic rGO hybrid aerogels for microwave absorption, infrared stealth and heat insulation. *Chem. Eng. J.* **2023**, *452*, 139376.

[55] Qiu, J. F.; Liao, J.; Wang, G. H.; Du, R. X.; Tsidaeva, N.; Wang, W. Implanting N-doped CQDs into rGO aerogels with diversified applications in microwave absorption and wastewater treatment. *Chem. Eng. J.* **2022**, *443*, 136475.

[56] Yang, D. D.; Dong, S.; Xin, J. Q.; Liu, C.; Hu, P. T.; Xia, L. S.; Hong, C. Q.; Zhang, X. H. Robust and thermostable C/SiOC composite aerogel for efficient microwave absorption, thermal insulation and flame retardancy. *Chem. Eng. J.* **2023**, *469*, 143851.

[57] Jin, L.; Wang, J. Q.; Wu, F.; Yin, Y. N.; Zhang, B. L. MXene@Fe_3O_4 microspheres/fibers composite microwave absorbing materials: Optimum composition and performance evaluation. *Carbon* **2021**, *182*, 770–780.

[58] Wu, F.; Liu, Z. H.; Wang, J. Q.; Shah, T.; Liu, P.; Zhang, Q. Y.; Zhang, B. L. Template-free self-assembly of MXene and CoNi-bimetal MOF into intertwined one-dimensional heterostructure and its microwave absorbing properties. *Chem. Eng. J.* **2021**, *422*, 130591.

[59] Xia, L.; Zhang, X. Y.; Yang, Y. N.; Zhang, J.; Zhong, B.; Zhang, T.; Wang, H. T. Enhanced electromagnetic wave absorption properties of laminated SiCNW-Cf/lithium–aluminum–silicate (LAS) composites. *J. Alloys Compd.* **2018**, *748*, 154–162.

[60] Zheng, Q.; Wang, J. Q.; Yu, M. J.; Cao, W. Q.; Zhai, H. Z.; Cao, M. S. Heterodimensional structure porous nanofibers embedded confining magnetic nanocrystals for electromagnetic functional material and device. *Carbon* **2023**, *210*, 118049.

[61] Cai, Z.; Ma, Y. F.; Zhao, K.; Yun, M. C.; Wang, X. Y.; Tong, Z. M.; Wang, M.; Suhr, J.; Xiao, L. T.; Jia, S. T. et al. $Ti_3C_2T_x$ MXene/graphene oxide/Co_3O_4 nanorods aerogels with tunable and broadband electromagnetic wave absorption. *Chem. Eng. J.* **2023**, *462*, 142042.

[62] Fang, G.; Wu, Y.; Xu, G. Y.; Peng, X. L.; Li, Y. P.; Zhang, Y. J.; Liu, C. Y. Data-driven oriented diatomic doping strategy to customize frequency dispersion for considerable microwave absorption. *J. Colloid Interface Sci.* **2024**, *654*, 327–338.

[63] Liu, J. L.; Zhang, L. M.; Wu, H. J.; Zang, D. Y. Boosted electromagnetic wave absorption performance from vacancies, defects and interfaces engineering in Co(OH)F/$Zn_{0.76}Co_{0.24}S$/Co_3S_4 composite. *Chem. Eng. J.* **2021**, *411*, 128601.

[64] Qin, M.; Zhang, L. M.; Wu, H. J. Dielectric loss mechanism in electromagnetic wave absorbing materials. *Adv. Sci.* **2022**, *9*, 2105553.

[65] Yang, Y. N.; Xia, L.; Zhang, T.; Shi, B.; Huang, L. N.; Zhong, B.; Zhang, X. Y.; Wang, H. T.; Zhang, J.; Wen, G. W. Fe_3O_4@LAS/RGO composites with a multiple transmission-absorption mechanism and enhanced electromagnetic wave absorption performance. *Chem. Eng. J.* **2018**, *352*, 510–518.

[66] Luo, J. H.; Dai, Z. Y.; Feng, M. N.; Chen, X. W.; Sun, C. H.; Xu, Y. Hierarchically porous carbon derived from natural Porphyra for excellent electromagnetic wave absorption. *J. Mater. Sci. Technol.* **2022**, *129*, 206–214.

[67] Zhang, S.; Liu, X. H.; Jia, C. Y.; Sun, Z. S.; Jiang, H. W.; Jia, Z. R.; Wu, G. L. Integration of multiple heterointerfaces in a hierarchical 0D@2D@1D structure for lightweight, flexible, and hydrophobic multifunctional electromagnetic protective fabrics. *Nano-Micro Lett.* **2023**, *15*, 204.

[68] Shen, Y. N.; Li, Q. H.; Xu, S. L.; Liu, X. Electromagnetic wave absorption of multifunctional cementitious composites incorporating polyvinyl alcohol (PVA) fibers and fly ash: Effects of microstructure and hydration. *Cem. Concr. Res.* **2021**, *143*, 106389.

[69] Liu, Y.; Liu, X. H.; E, X. Y.; Wang, B. B.; Jia, Z. R.; Chi, Q. G.; Wu, G. L. Synthesis of Mn_xO_y@C hybrid composites for optimal electromagnetic wave absorption capacity and wideband absorption. *J. Mater. Sci. Technol.* **2022**, *103*, 157–164.

[70] Li, L.; Wang, T. H.; Liu, Q. L.; Cao, Y. M.; Qiu, J. S. A high CO_2 permselective mesoporous silica/carbon composite membrane for CO_2 separation. *Carbon* **2012**, *50*, 5186–5195.

[71] Fang, G.; Liu, C. Y.; Xu, M.; Zhang, X. H.; Wu, Y.; Kim, D. H.; Ji, G. B. The elaborate design of multi-polarization effect by non-edge defect strategy for ultra-broad microwave absorption. *Adv. Funct. Mater.* **2024**, *34*, 2404532.

[72] Gong, X. Y.; Li, M.; Ge, Y.; Wang, E. H.; Liu, X. Z.; Chen, Z. Y.; Wang, J. H.; Bao, Z. Y.; Wu, Y. C. Enhanced low-frequency microwave absorption of N-doped biomass derived carbon. *Mater. Today Commun.* **2023**, *37*, 107093.

[73] Nelson, J. K.; Fothergill, J. C. Internal charge behaviour of nanocomposites. *Nanotechnology* **2004**, *15*, 586–595.

[74] Wang, G.; Li, C. F.; Estevez, D.; Xu, P.; Peng, M. Y.; Wei, H. J.; Qin, F. X. Boosting interfacial polarization through heterointerface engineering in MXene/graphene intercalated-based microspheres for electromagnetic wave absorption. *Nano-Micro Lett.* **2023**, *15*, 152.

[75] Wu, Y.; Zhao, Y.; Zhou, M.; Tan, S. J.; Peymanfar, R.; Aslibeiki, B.; Ji, G. B. Ultrabroad microwave absorption ability and infrared stealth property of Nano-Micro CuS@rGO lightweight aerogels. *Nano-Micro Lett.* **2022**, *14*, 171.

This is an open access article under the terms of the Creative Commons Attribution 4.0 International License (CC BY 4.0, https://creativecommons.org/licenses/by/4.0/).

© The Author(s) 2025. Published by Tsinghua University Press.